

Article

Insights into SnO₂ Nanoparticles Supported on Fibrous Mesoporous Silica for CO Catalytic Oxidation

Guobo Li ¹, Yingying Zhang ¹, Jie Yan ¹, Yiwei Luo ¹, Conghui Wang ², Weiwei Feng ¹, Shule Zhang ³, Wenming Liu ², Zehui Zhang ^{4,*} and Honggen Peng ^{1,*} 

¹ School of Resources and Environment, Nanchang University, Nanchang 330031, China; liguobo@ncu.edu.cn (G.L.); zhangyingying0326@163.com (Y.Z.); 19914754363@163.com (J.Y.); lyw243757814@163.com (Y.L.); fengweiwei@email.ncu.edu.cn (W.F.)

² School of Chemistry and Chemical Engineering, Nanchang University, Nanchang 330031, China; conghuiwang2022@163.com (C.W.); wmliu@ncu.edu.cn (W.L.)

³ School of Chemical Engineering, Nanjing University of Science and Technology, Nanjing 210094, China; shulezhang@163.com

⁴ School of Chemistry and Materials Science, Central South National University, Wuhan 430074, China

* Correspondence: zehuizh@mail.ustc.edu.cn (Z.Z.); penghonggen@ncu.edu.cn (H.P.); Tel.: +86-0791-8396-9583 (H.P.)

Abstract: A large surface area dendritic mesoporous silica material (KCC-1) was successfully synthesized and used as a support to confine SnO₂ nanoparticles (NPs). Owing to the large specific surface area and abundant mesoporous structure of dendritic KCC-1, the SnO₂ NPs were highly dispersed, resulting in significantly improved CO catalytic oxidation activity. The obtained Sn_x/KCC-1 catalysts (*x* represents the mass fraction of SnO₂ loading) exhibited excellent CO catalytic activity, with the Sn₇@KCC-1 catalyst achieving 90% CO conversion at about 175 °C. The SnO₂ NPs on the KCC-1 surface in a highly dispersed amorphous form, as well as the excellent interaction between SnO₂ NPs and KCC-1, positively contributed to the catalytic removal process of CO on the catalyst surface. The CO catalytic removal pathway was established through a combination of in situ diffuse reflectance infrared transform spectroscopy and density-functional theory calculations, revealing the sequential steps: ① CO → CO₃²⁻_{ads}, ② CO₃²⁻_{ads} → CO₂_{free} + SnO_{x-1}, ③ SnO_{x-1} + O₂ → SnO_{x+1}. This study provides valuable insights into the design of high-efficiency non-precious metal catalysts for CO catalytic oxidation catalysts with high efficiency.

Keywords: CO catalytic oxidation; SnO₂ nanoparticles; DFT; reaction mechanism



Citation: Li, G.; Zhang, Y.; Yan, J.; Luo, Y.; Wang, C.; Feng, W.; Zhang, S.; Liu, W.; Zhang, Z.; Peng, H. Insights into SnO₂ Nanoparticles Supported on Fibrous Mesoporous Silica for CO Catalytic Oxidation. *Catalysts* **2023**, *13*, 1156. <https://doi.org/10.3390/catal13081156>

Academic Editors: Zichuan Ma, Xing Zhou and Carlo Santoro

Received: 2 June 2023

Revised: 12 July 2023

Accepted: 24 July 2023

Published: 26 July 2023



Copyright: © 2023 by the authors. Licensee MDPI, Basel, Switzerland. This article is an open access article distributed under the terms and conditions of the Creative Commons Attribution (CC BY) license (<https://creativecommons.org/licenses/by/4.0/>).

1. Introduction

Carbon monoxide (CO) is one of the six basic control pollutant items in China's "environmental air quality standards". It mainly originates from metallurgical, chemical, and other industries, fossil fuel combustion, waste incineration, and automobile exhaust [1,2]. In sintering flue gas, the concentration of CO can reach 1~3%. It is well known that carbon monoxide (CO) emissions from automobiles and industries are poisonous and harmful gases with adverse effects on the human body, atmosphere, and ecosystem. The catalytic oxidation of CO has been recognized as an extremely effective approach for CO elimination, and it is crucial to design a low-temperature high-efficiency catalyst material to enhance CO catalytic oxidation.

Catalysts are the core of CO catalytic oxidation technology, which significantly affects catalytic activity, and are generally divided into precious metal and non-noble metal catalysts [3,4]. Noble metals, such as Pt and Au, have been widely used as critical active components in CO emission control catalysts owing to their excellent conclusive activity for CO oxidation [5–7]. Precious metal catalysts exhibit outstanding CO adsorption and activation properties. However, their widespread application is limited owing to resource

scarcity and high prices. Non-noble metal catalysts, particularly transition metal catalysts, such as SnO₂ [8], CuO [9,10], Co₃O₄ [11], Mn₃O₄ [12], and CeO₂ [8,13], also demonstrate high activity in the catalytic oxidation reaction of CO. Among them, tin (Sn)-based catalysts have garnered more attention owing to their excellent catalytic activity and stability, which are comparable to those of precious metals. SnO₂ is an efficient gas sensor material with unique optical, catalytic, and electrical properties and high-temperature stability, making it suitable for catalysis, energy storage, and other applications. Zhao et al. [14] reported that an Sn-modified Pd-Cu/APT catalyst exhibited superior catalytic performance for CO oxidation under moisture-rich conditions. Peng et al. [15] demonstrated that mesoporous SnO₂ nanosheet materials with a higher surface area, larger pore volume, and more active surface oxygen species showed excellent catalytic activity for CO oxidation. However, in CO catalytic reactions, both precious metal and non-noble metal catalysts are often susceptible to the agglomeration of nanoparticles (NPs), which are the active components. To address this issue, several catalyst construction strategies have been suggested [16]: (i) restriction of NPs' steric by one-dimensional metal oxides (such as carbon nanotubes) [17,18]; (ii) embedding NPs into the silica matrix or porous shell [19,20]; (iii) supported NPs within mesoporous material channels, such as SBA-15 [21,22] and MCM-41 [23]; (iv) stably anchoring NPs to the catalyst surface through strong metal–support interactions [24]. The confinement strategies mentioned above effectively reduce the sintering of active NP components and significantly enhance catalytic stability. However, typical confinement techniques, such as porous or core–shell arrangements, may hinder reactant transport to some extent or sacrifice certain active centers [25]. Therefore, a better strategy for confining active components is needed to achieve a catalyst with superior CO removal performance.

In this study, a series of Sn_x/KCC-1 catalysts with well-dispersed Sn atomic clusters were synthesized. They achieved CO catalytic performances comparable to those of noble-metal catalysts. The synthesized catalysts and Sn₇/MCM-41 catalysts were contrasted. The high dispersion of Sn atomic clusters on KCC-1 was achieved through favorable electron interaction and anchoring effects. The interaction of the Sn_x/KCC-1 catalyst with CO and O₂ gas molecules was investigated through various characterization methods, such as XPS, H₂-TPR, O₂-TPD, etc. Additionally, the reaction intermediates and CO transient reaction process on the catalyst surface were characterized through a combination of in situ diffuse reflectance infrared Fourier-transform spectroscopy (in situ DRIFTS) and density functional theory (DFT); thus, the CO catalytic oxidation removal path was finally established.

2. Discussion

2.1. Basic Morphological Characteristics

The morphologies of KCC-1, Sn₇@KCC-1, Sn₇@MCM-41, and pure SnO₂ catalysts were investigated via SEM. The SEM image (Figure 1d) shows that the pure SnO₂ active components were agglomerated microspheres. Figure 1a,b reveals that KCC-1 featured a fibrous microsphere morphology resembling flowers, with an average spherical diameter of ~1500 nm. This morphology remained largely unchanged after SnO₂ loading. This structure was conducive to heterogeneous catalytic reactions occurring on the catalyst surface. In the case of the Sn₇@MCM-41 catalyst (Figure 1c), the SnO₂ particles were distributed within the MCM-41 support, with slight agglomeration.

2.2. Evaluation of Catalytic Activity

The CO catalytic oxidation performance of pure SnO₂, Sn₇@KCC-1, and Sn₇@MCM-41 catalysts was evaluated, and the results are shown in Figure 2a. The Sn₇@KCC-1 catalyst exhibited a better CO catalytic activity than that of SnO₂ and Sn₇@MCM-41 catalysts, with over 90% CO conversion achieved over 175 °C. As displayed in Figure 2b, the Sn_x@KCC-1 catalysts exhibited excellent CO catalytic activity, especially the Sn₇@KCC-1 catalyst, indicating that flower-like fibrous microspheres were beneficial to the heterogeneous catalytic reaction. The CO conversion of Sn₁₀@KCC-1 was lower than that of Sn₇@KCC-1, which may be caused by the aggregation of high-content active components, which was also

shown in other reported catalysts [26,27]. The CO conversion stability of the $\text{Sn}_x\text{@KCC-1}$ catalyst was conducted at 200 °C, and the result is presented in Figure S1. After a 25 h test, almost no reduction in CO catalytic activity for the $\text{Sn}_7\text{@KCC-1}$ catalyst was found, indicating excellent stability.

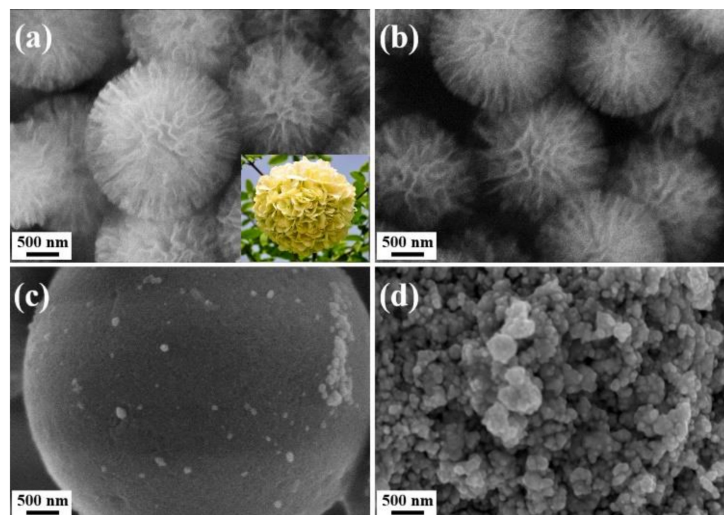


Figure 1. SEM images of (a) KCC-1, (b) $\text{Sn}_7\text{@KCC-1}$, (c) $\text{Sn}_7\text{@MCM-41}$, and (d) pure SnO_2 catalysts.

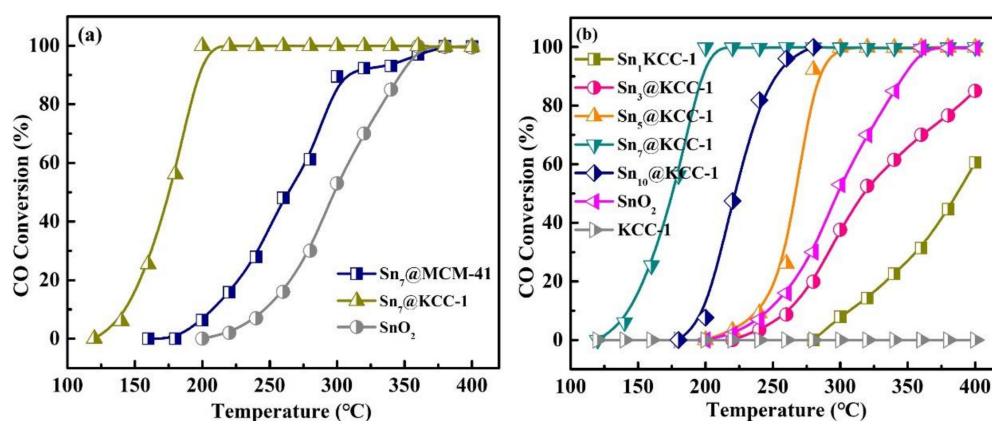


Figure 2. Catalytic performance of (a) pure SnO_2 , $\text{Sn}_7\text{@KCC-1}$, and $\text{Sn}_7\text{@MCM-41}$, and (b) $\text{Sn}_x\text{@KCC-1}$ catalysts with different content of SnO_2 for CO oxidation, respectively. Reaction conditions: 1% CO, 21% O_2 , balanced by N_2 , and WHSV = 18,000 mL $\text{g}_{\text{cat}}^{-1} \text{h}^{-1}$.

The lattice structures of $\text{Sn}_x\text{@KCC-1}$ and related catalysts were analyzed via XRD, and the results are shown in Figure 3. Strong diffraction peaks corresponding to different crystal faces of pure SnO_2 , such as (110), (101), (220), and (211), were observed. Additionally, the $\text{Sn}_x\text{@KCC-1}$ catalysts featured a broad diffraction peak at a 2θ value of 22.58, attributable to the typical diffraction peak of the amorphous SiO_2 present in the mesoporous molecular sieve KCC-1 [16]. These results suggested that SnO_2 existed on the surface of KCC-1 in an amorphous form, which was conducive to CO catalytic removal on the catalyst surface.

The morphology and pore structure of $\text{Sn}_x\text{@KCC-1}$ catalysts play a crucial role in heterogeneous catalysis. No distinct lattice structures for KCC-1 and SnO_2 were observed in the high-resolution transmission electron micrographs of $\text{Sn}_7\text{@KCC-1}$, $\text{Sn}_7\text{@MCM-41}$, and pure SnO_2 catalysts (Figure 4). This indicates that the SnO_2 NPs were uniformly dispersed within the KCC-1 and/or MCM-41 support, particularly within KCC-1. This uniform dispersion ensured effective contact between the catalyst surface's active component and gas molecules (CO and O_2). Additionally, the high-angle annular dark-field scanning transmission electron microscopy and energy-dispersive X-ray spectroscopy mapping

results (Figure S2) revealed well-distributed SnO₂ NPs on KCC-1, demonstrating the nonexistence of active component accumulation. The mesoporous molecular sieve KCC-1 exhibited a unique fibrous structure (flower-like fibrous microspheres). This structure allowed the SnO₂ NPs to be supported on the surface of the fibrous structure rather than in the pores, resulting in smaller particle sizes for the SnO₂ NPs, with some even less than 10 nm, which was an advantage of the KCC-1 molecular sieve compared with MCM-41. Consequently, the Sn_x@KCC-1 catalysts exhibited excellent CO catalytic activity.

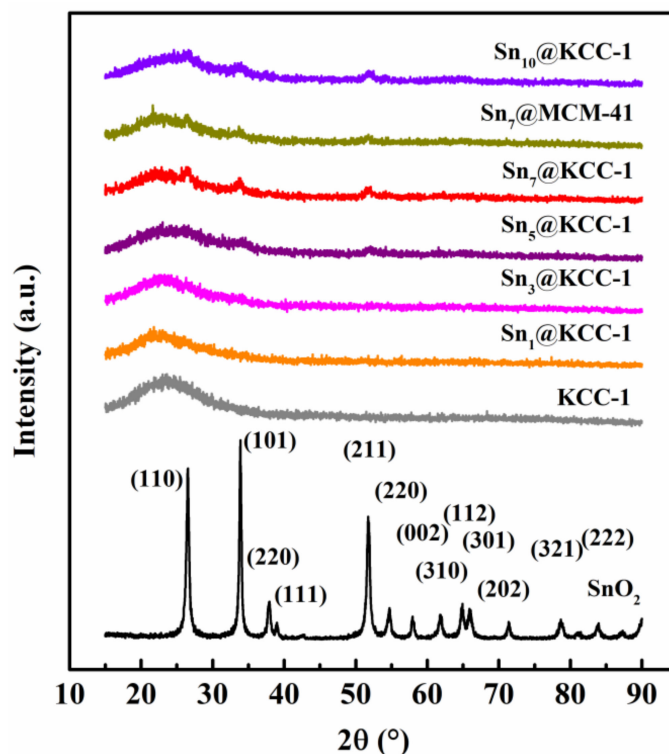


Figure 3. XRD patterns of Sn_x@KCC-1 and related catalyst materials.

The nitrogen (N₂) adsorption–desorption isotherms and corresponding BJH pore size distribution curves of SnO₂, KCC-1, SnO_x/KCC-1, and Sn₇@MCM-41 catalysts in the relative pressure (P/P_0) range of 0.05–0.25 are presented in Figure 5, and the analysis results are listed in Table 1. According to the classification by the International Union of Pure and Applied Chemistry (IUPAC), the adsorption–desorption isotherms of Sn_x@KCC-1 belonged to type IV, with a typical H3-type hysteresis loop, while the hysteresis loop of Sn₇@MCM-41 was H2-type [28,29]. Table 1 provides the specific surface area and pore volume data. Pure SnO₂ featured a low specific surface area of only 19 m²/g and a small pore volume of 0.16 cm³/g. In contrast, KCC-1 exhibited a significantly higher specific surface area of 552 m²/g and a maximum pore volume of 1.93 cm³/g. MCM-41 exhibited an even higher specific surface area of 1216 m²/g and a pore volume of 0.96 cm³/g, exceeding that of pure SnO₂. When doped with SnO₂ NPs, both Sn_x@KCC-1 and Sn₇@MCM-41 showed a decrease in specific surface area, pore volume, and pore size compared to their non-doped counterparts. Specifically, as the doping of SnO₂ NPs increased from 1% to 10%, the specific surface area of Sn_x@KCC-1 decreased from 529 to 269 m²/g, and the pore volume decreased from 1.91 to 0.95 cm³/g. Analysis of the pore size distribution of Sn_x@KCC-1 revealed the presence of two distinct pore sets: a unique mesoporous pore with a size of 2.7 nm embedded within the flower-like fibrous microspheres structure of the KCC-1 molecular sieve and a surface layer stacked pore with a size of 20 nm.

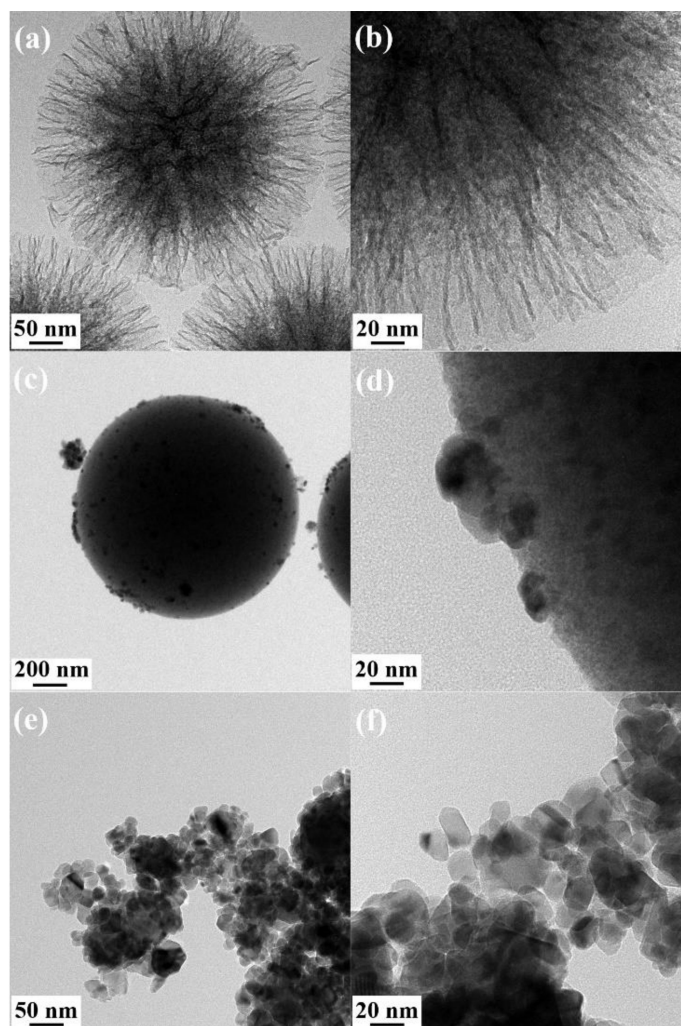


Figure 4. TEM images of (a,b) $\text{Sn}_7\text{@KCC-1}$, (c,d) $\text{Sn}_7\text{@MCM-41}$, and (e,f) pure SnO_2 .

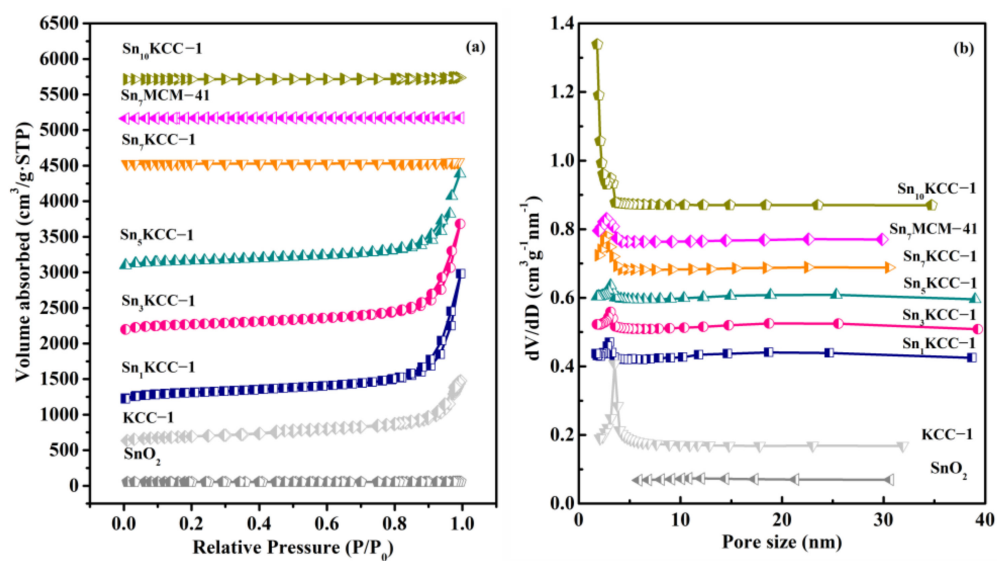


Figure 5. (a) N_2 adsorption–desorption isotherms and (b) pore size distribution curves of $\text{SnO}_x/\text{KCC-1}$ and related catalyst materials.

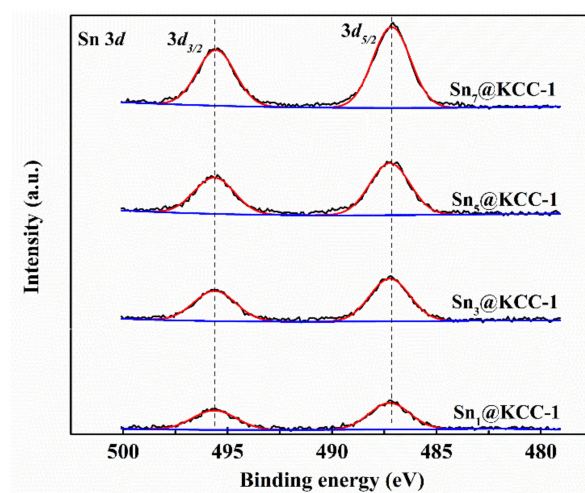
Table 1. Textural parameters of SnKCC-1 and related materials.

Catalyst Samples	Surface Area (m ² /g) ^a	Pore Volume (cm ³ /g) ^b	Pore Size (nm) ^b
KCC-1	552	1.93	3.5
MCM-41	1216	0.96	3.2
Sn ₁ @KCC-1	529	1.91	2.7
Sn ₃ @KCC-1	499	1.74	2.7
Sn ₅ @KCC-1	422	1.53	2.7
Sn ₇ @KCC-1	315	0.96	2.7
Sn ₁₀ @KCC-1	269	0.95	2.7
Sn ₇ @MCM-41	807	0.61	2.9
SnO ₂	19	0.16	10.4

^a: determined from the linear part of BET equation ($P/P_0 = 0.05-0.25$). ^b: determined from BJH equation.

The reducibility of the prepared Sn_x@KCC-1 catalysts was investigated via the H₂-TPR technique. As shown in Figure S3, consistent with previous findings, a single wide peak was observed around 703.4 °C for pure SnO₂, corresponding to the reduction of Sn⁴⁺ to Sn⁰ [27]. The reduction peak temperature of Sn_x/KCC-1 catalysts was ~100 °C lower than that of pure SnO₂, indicating excellent redox properties of the catalysts. The lower reduction temperature suggests that CO oxidation was more likely to occur on the Sn_x/KCC-1 catalyst surface.

To further examine the oxidation state of SnO₂ in the Sn_x@KCC-1 catalysts, XPS analysis was performed on the samples before and after CO oxidation cycles. XPS is a surface-sensitive technique that provides information about the chemical states of components on the catalyst surface. The Sn 3d XPS spectra are shown in Figure 6. The doublet peaks observed at binding energies of approximately 495.5 and 487.1 eV correspond to Sn 3d_{3/2} and 3d_{5/2} for Sn⁴⁺ species, respectively [30]. The binding energies of both peaks for the different SnO₂ loadings remained nearly unchanged, indicating that increasing the SnO₂ loading did not alter the chemical states of Sn species on the Sn_x@KCC-1 catalyst surface. Moreover, as the SnO₂ loading increased, the amount of Sn⁴⁺ species on the Sn₇@KCC-1 catalyst reached its highest value, consistent with the H₂-TPR results. These Sn species are considered active centers for activating reactants (CO and O₂); hence, having a greater abundance of Sn species with higher positive valences promotes the catalytic oxidation of CO.

**Figure 6.** The Sn 3d XPS survey scans spectra of Sn_x@KCC-1 catalysts.

2.3. Adsorption of CO and O₂ on SnO₂ (110) Catalyst Surface

The optimized structure of the SnO₂ (110) catalyst (Figure 7) reveals the intriguing nature of the SnO₂ surfaces, which exhibited two potential oxidation states of tin (+2

and +4), reduced atomic coordination, and advantageous compositional alterations and reconstructions. According to the calculated results, the surface Sn and O atoms were likely the adsorption sites for CO and O₂ gas molecules. The use of non-precious metal (SnO₂) in the catalytic oxidation of CO serves as a design principle for the development of advanced catalytic systems with a wide range of applications.

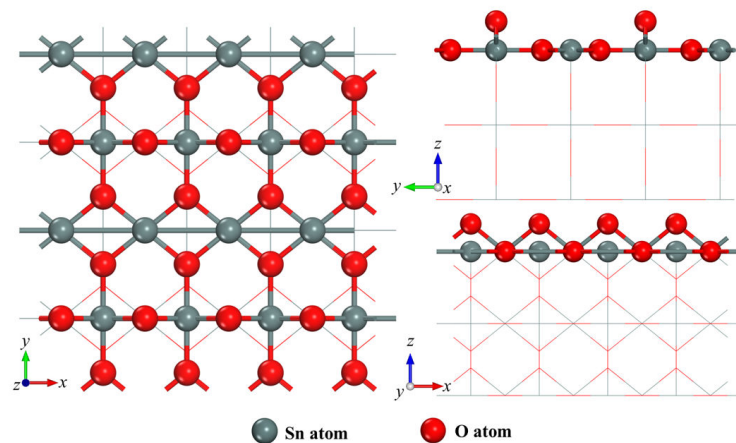


Figure 7. Top and side view of optimized SnO₂ (110) catalyst structure.

During CO catalytic oxidation, the adsorption of CO and O₂ on the surface of the SnO₂ (110) catalyst played a crucial role. Therefore, the adsorption of CO and O₂ on the SnO₂ (110) surface was investigated separately (Figure 8). Single O₂ molecule adsorption was observed around the Sn active center on the SnO₂ (110) surface. The formed Sn–O bond featured a length of 2.147 Å, with an adsorption energy of −6.14 eV. According to the projected density of states (PDOS) results, in the adsorption configurations of both CO and O₂, the highest occupied molecular orbital of O₂ hybridized with the lowest unoccupied molecular orbital of Sn. CO, as the most important reactant, exhibited an adsorption energy value of −1.678 eV on the Sn surface, resulting in the generation of CO₃^{2−} species. The lengths of the newly formed C–O bonds were 2.116 Å and 2.121 Å, respectively. The PDOS analysis confirmed that the adsorption of these gas molecules on the SnO₂ (110) surface involved chemisorption, indicating their effective activation by the catalyst surface. Therefore, CO can be efficiently converted on the SnO₂ (110) catalyst surface.

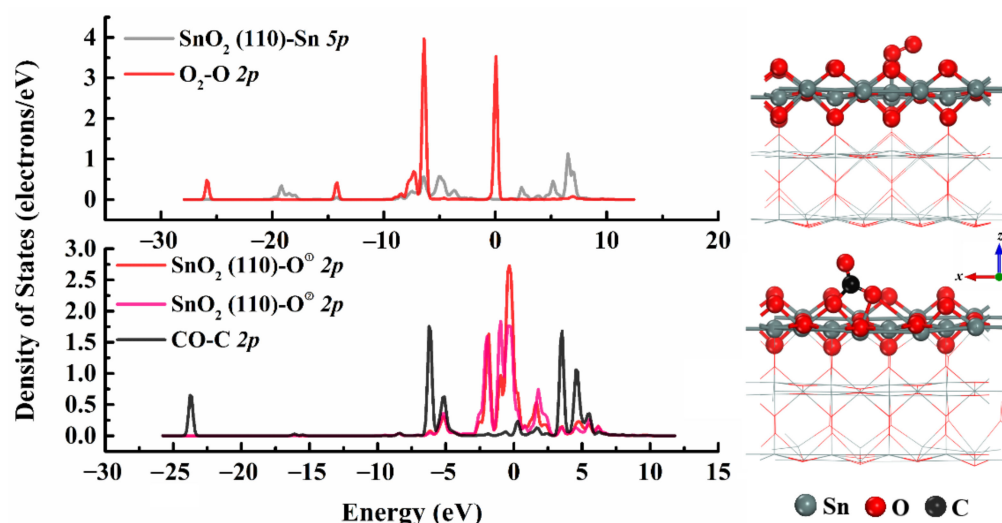


Figure 8. Optimized adsorption configurations and projected density of states (PDOS) on SnO₂ (110) catalyst surface for O₂ and CO molecules, respectively.

2.4. Instantaneous Intermediates on the Catalysts

To further investigate the instantaneous intermediates of the CO + O₂ catalytic oxidation reaction on the Sn₇@KCC-1 catalyst surface, a transient CO + O₂ adsorption experiment was conducted at 200 °C. Figure 9 presents the CO + O₂ reaction spectra of the Sn₇@KCC-1 catalyst. The peaks at approximately 2119 and 2173 cm⁻¹ can be attributed to the linearly adsorbed CO species on surface Sn⁴⁺ centers (Sn⁴⁺-CO) [31]. These results indicate that CO was readily adsorbed on the surface of the Sn₇@KCC-1 catalyst with 7% SnO₂, forming active intermediates. This finding is consistent with the DFT calculation results (Figure 8). The identified species on the Sn₇@KCC-1 catalyst surface suggest that the catalytic oxidation of CO predominantly followed the Mars–van Krevelen (MvK) mechanism.

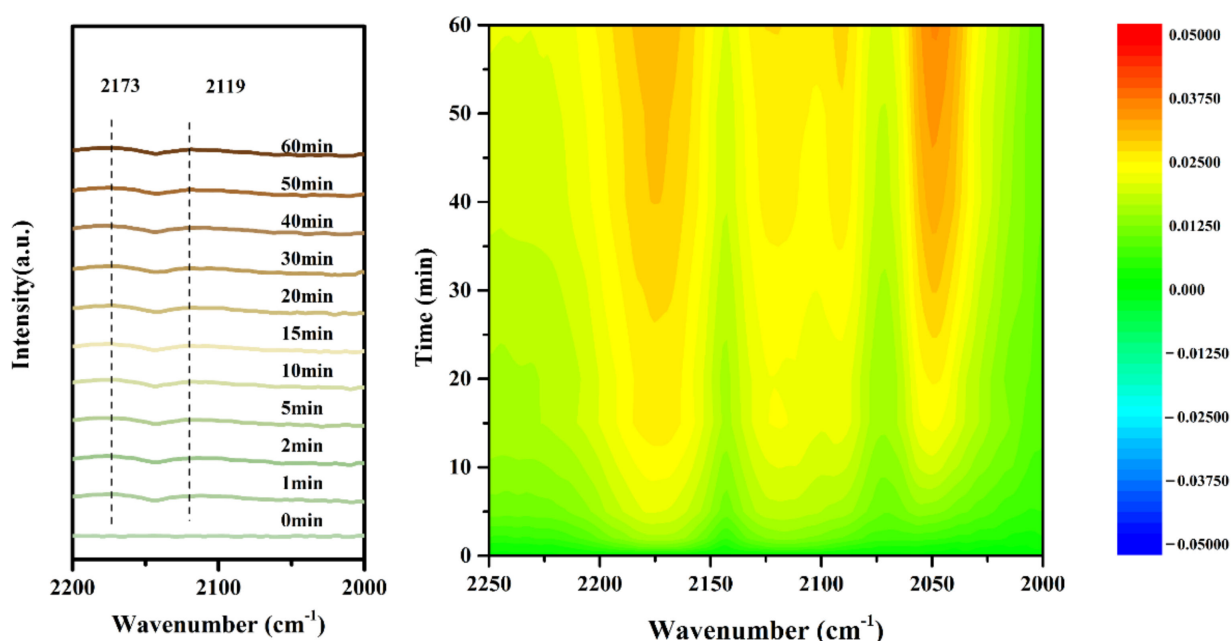


Figure 9. The transient CO + O₂ reaction DRIFTS profiles of Sn₇@KCC-1 catalyst measured at 200 °C; the right figures are the mapping results derived from the DRIFTS profiles.

The CO removal step reaction process on the SnO₂ (110) catalyst surface was further explored through DFT calculations. The obtained transient CO + O₂ reaction DRIFTS profiles of Sn₇@KCC-1 catalyst results are shown in Figure 10. The detailed reaction pathway was as follows: ① CO → CO₃²⁻_{ads}, ② CO₃²⁻_{ads} → CO₂_{free} + SnO_{x-1}, ③ SnO_{x-1} + O₂ → SnO_{x+1}. As shown in Figure 10, CO gas molecules first adsorbed onto the SnO₂ (110) surface, forming the CO₃²⁻ species. Subsequently, CO₂ was dissociated from the SnO₂ (110) catalyst surface; this process was accompanied by the formation of an oxygen vacancy structure (SnO_{x-1}). This step, with a reaction energy (Er) of 5.362 eV, may determine the rate of CO catalytic oxidation. The physicochemical properties of the catalyst remained unchanged before and after the chemical reaction. Therefore, the SnO_{x-1} structure was restored through the oxidation of O₂ gas molecules. In summary, the catalytic oxidation of CO on the SnO₂ (110) surface followed the MvK mechanism. The CO gas molecule reacted with the lattice oxygen (O_{latt}) on the SnO₂ (110) surface, forming CO₃²⁻ species. Subsequently, CO₂ was dissociated from the SnO₂ (110) catalyst, and gaseous O₂ refilled the oxygen vacancy, leading to the restoration of the catalyst. These findings are consistent with the literature reports [32].

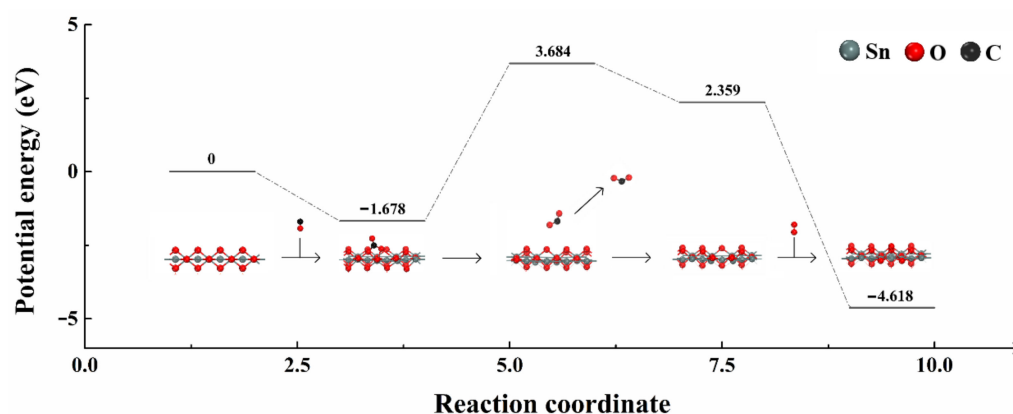


Figure 10. Removal path and energy barrier of CO on the SnO₂ (110) catalyst surface.

3. Conclusions

A series of Sn_x@KCC-1 catalysts were prepared by loading SnO₂ NPs onto flower-like fibrous microspheres of mesoporous silica (KCC-1), in which the SnO₂ NPs were supported and highly dispersed. The obtained Sn_x/KCC-1 catalysts exhibited excellent CO catalytic activity, with the Sn₇@KCC-1 catalyst showing the highest performance, achieving 90% CO conversion at ~175 °C. KCC-1 exhibited a significantly larger specific surface area of 552 m²/g and a maximum pore volume of 1.93 cm³/g. The SnO₂ NPs on the KCC-1 surface were highly dispersed in an amorphous form, and the strong interaction between SnO₂ NPs and KCC-1 contributed to the catalytic removal of CO on the catalyst surface. The presence of Sn⁴⁺ species as active centers facilitated the activation of CO and O₂, thereby promoting the catalytic oxidation of CO. The CO catalytic removal pathway was established through a combination of in situ DRIFTS and DFT calculations. The oxidation of CO on the SnO₂ (110) surface followed the MvK mechanism, with the detailed reaction pathway as follows: ① CO → CO₃²⁻_{ads}, ② CO₃²⁻_{ads} → CO₂_{free} + SnO_{x-1}, ③ SnO_{x-1} + O₂ → SnO_{x+1}. This study provides valuable insights into the design of high-efficiency non-precious metal catalysts for CO catalytic oxidation.

4. Experimental

4.1. Catalyst Preparation

The required reagents were supplied by Sinopharm Chemical Reagent Co., Ltd. (Beijing, China). The KCC-1 [33] and MCM-41 [34] supports were prepared according to previously reported procedures.

The detailed preparation process of the KCC-1 support was as follows. First, 60 mL of cyclohexane (99.50%), 3.00 mL of n-pentanol (99.50%), and 5.00 g of tetraethyl orthosilicate (TEOS, 99%, 18.92 mmol) were mixed at 25 °C to obtain liquid A. Then, 2.00 g of cetyltrimethylammonium bromide (CTAB, 99%, 5.48 mmol) and 1.20 g of urea (99%, 19.98 mmol) were dissolved in 60 mL of deionized water to obtain liquid B. Liquid B was slowly poured into liquid A, and the resulting solution was thoroughly mixed. The mixture was then transferred into a stainless steel autoclave, sealed, and maintained at 120 °C for 6 h with constant stirring. After cooling to 25 °C, the precipitation was collected by filtering and washing with acetone (99.50%) and ethanol (99.50%). Then, the final precipitation was dried at 80 °C overnight and calcined in a muffle furnace at 550 °C for 6 h to remove the template agent (the heating 2 °C·min⁻¹). Finally, the white powder of mesoporous molecular sieve material KCC-1 was obtained.

The detailed preparation process of the MCM-41 support was as follows. Cetyltrimethylammonium bromide, as the mesoporous directing agent, was dissolved in water and stirred until it became colorless. Tetraethyl orthosilicate as the Si source was added to the mixture after 30 min. The pH value of this gel mixture was adjusted to 10 by adding NH₃·H₂O. After being stirred for 3 h, the gel solution was further aged and crystallized at 65 °C for

18 h in an oven. Finally, the solution was filtered, washed with ultrapure water until the pH reached 7, dried, and calcined at 550 °C for 6 h.

The detailed preparation process of the Sn_x/KCC-1 support was as follows. First, 0.50 g of KCC-1 (or MCM-41) supports was impregnated in a solution containing 10.00 mL of ethylene glycol (99.50%) and the appropriate amount of Sn(NO₃)₄·6H₂O (≥99.00%). The resulting solid–liquid mixture was dried in a vacuum oven at 80 °C until the solvent completely evaporated. Then, the resulting solid was calcined in a tube furnace at 550 °C in an N₂ atmosphere for 4 h. Finally, the atmosphere was switched to air and maintained at 550 °C for 2 h. The obtained catalysts were named Sn_x/KCC-1 (or Sn_x@MCM-41) catalyst, where *x* represents the mass fraction of SnO₂ loading.

For comparison, pristine SnO₂ without a three-dimensional spatial structure was prepared through a homogeneous precipitation method. In a typical process, an appropriate amount of Sn(NO₃)₄·6H₂O (≥99.00%) was first dissolved in deionized water (with a Sn⁴⁺ concentration of 0.1 mol·L^{−1}). After 30 min of stirring, ammonia solution (Sinopharm, 25–28 wt.%) was added dropwise to the solution until the pH reached ~10. The mixture was stirred at 25 °C for 3 h. Finally, the precipitate was filtered, washed, dried, and calcined using the same calcination procedures as mentioned above.

4.2. Evaluation of the Catalytic Performance

The CO catalytic oxidation ability of the obtained catalysts was tested in a self-assembled fixed-bed quartz reactor with continuous flow. Furthermore, the Weisz–Prater Criterion was used to assess the effectiveness of internal diffusion. The CO oxidation activity tests were evaluated in a fixed-bed quartz reactor using a U-shaped quartz tube with an inner diameter of 6 mm under the following typical reaction condition: [CO] = 1 vol.%, [O₂] = 21 vol.%, N₂ as balance gas with a total flow rate of 30 mL min^{−1}, and the catalyst mass for each test is 50 mg. GC9310 gas chromatograph (equipped with a TDX-01 column and a TCD detector) and N-2000 workstation were used for collecting and analyzing the reactants and products. The conversion of CO (*X*_{CO}) was calculated using Equation (1):

$$X_{\text{CO}} = \left(1 - \frac{S_{\text{CO-outlet}}}{S_{\text{CO-inlet}}}\right) \times 100\% \quad (1)$$

where *S*_{CO-outlet} and *S*_{CO-inlet} are the CO concentration in the inlet and outlet gas streams corresponding to the CO inlet and outlet peak areas, respectively, which are derived from the gas chromatograph responses using the modified area normalization method.

4.3. Catalyst Characterization

Powder X-ray diffraction (XRD) patterns of the catalysts were obtained using a Rigaku SmartLab 9 kW (Tokyo, Japan) diffractometer with Cu Kα radiation (λ = 1.5418 Å). The instrument was operated at 40 kV and 150 mA, and scans were collected in the 2θ range from 10° to 90°, with a step of 2° min^{−1} to analyze the phase structure. The specific surface areas of the catalysts were determined through nitrogen adsorption experiments at 77 K using a Micromeritics ASAP2020 instrument (Micromeritics Corporate, Norcross, GA, USA). Prior to the test, 100 mg of catalyst was degassed at 300 °C for 5 h. Nitrogen adsorption and desorption were then performed to obtain the N₂ adsorption–desorption curve. The specific surface areas of the samples were calculated through the Brunauer–Emmett–Teller (BET) method in the relative pressure (*p*/*p*₀) range of 0.05–0.25. The pore size distributions of the samples were calculated through the Barrett–Joyner–Halenda (BJH) method. Scanning electron microscopy (SEM) and transmission electron microscopy images were captured using a Hitachi S-4800 field emission scanning electron microscope (Hitachi Ltd, Tokyo, Japan) and a Tecnai™ F30 transmission electron microscope (Fei company, Hillsboro, OR, USA), respectively. XPS was performed using a PHI-5000C ESCA system (PerkinElmer, Waltham, MA, USA) with a single Mg-K X-ray source operated at 250 W and 14 kV. The spectra were obtained at ambient temperature under ultrahigh vacuum conditions. The binding energies were calibrated using the standard C 1s peak of graphite at 284.8 eV. In situ

DRIFTS experiments were conducted using an is50 spectrometer equipped with a liquid nitrogen-cooled mercury cadmium telluride A (MCT-A) detector and a Harrick Scientific DRIFTS cell. Prior to each test, each sample was pretreated at 400 °C for 60 min under a N₂ flow of 30 mL·min⁻¹. The background spectrum at the desired temperature was collected after pretreatment in an N₂ atmosphere, which was deduced from the sample spectra for each measurement. For the in situ transient reactions of pre-adsorbed CO, the catalysts were exposed to 1% CO/N₂ (30 mL·min⁻¹) for adsorption at 100 °C after pretreatment. After half an hour, the catalyst was purged with N₂ for 10 min. Then, the sample was subjected to a flow of 21% O₂/N₂ (30 mL·min⁻¹), and the reaction process was recorded as a function of time.

4.4. DFT Calculation

The Vienna Ab-initio Simulation Package (VASP) was adopted for the density functional theory (DFT) calculations [35–37]. The Projector Augmented Wave (PAW) method was used to solve the Kohn–Sham equations [38]. The generalized gradient approximation and Perdew–Burke–Ernzerhof (GGA-PBE) exchange association functional were adopted [39]. A dipole correction was introduced to describe the total energy and eliminate dipole moment, which is caused by metal atoms adsorption [40].

During the adsorption calculations, a kinetic energy cutoff of 500 eV was used. A Gamma-centered 1 × 1 × 1 mesh was employed for Brillouin zone integration. Geometry optimization was performed using the whole ad-molecule model relaxation. A vacuum layer with a thickness of at least 20 Å in the z-direction was added to simulate the surfaces and ensure that the reaction was not influenced by the next layer. The convergence criteria for electronic and geometry relaxation were set to 10⁻⁵ eV and 0.01 eV·Å⁻¹, respectively. Adsorption was allowed on only one side of the exposed surface, and the dipole moment was corrected accordingly in the z-direction. The adsorption energy (E_{ads}) of reaction gas on the SbPdV/N-TiO₂ (101) surface was calculated using Equation (2):

$$E_{ads} = E_{gas-structure} - (E_{gas} + E_{structure}) \quad (2)$$

where E_{ads} , $E_{structure}$, and E_{gas} are the total energies of adsorbed reaction gas over SnO₂ structure (110) surface, interacting SnO₂ (110) structure surface, and the isolated gas molecules in vacuum, respectively.

The reaction energy (E_r) is defined as Equation (3):

$$E_r = E_{FS} - E_{IS} \quad (3)$$

E_{IS} and E_{FS} are the energies of the initial and final states, respectively.

Supplementary Materials: The following supporting information can be downloaded at: <https://www.mdpi.com/article/10.3390/catal13081156/s1>. Evaluation of the catalytic performance. Figure S1: CO conversion stability at 200 °C of Sn₇@KCC-1 catalyst in the condition of 1% CO + 21% O₂, balanced by N₂, and WHSV = 18,000 mL g_{cat}⁻¹ h⁻¹. Figure S2: HAADF-STEM and EDX-mapping of Sn₇@KCC-1. Figure S3: H-TPR of Sn₁@KCC-1, Sn₁@KCC-1 and SnO₂ catalysts.

Author Contributions: Conceptualization by G.L. and Y.Z.; supervision by Y.Z. and J.Y.; writing—original draft by J.Y., Y.L., C.W. and W.F.; writing—review and editing by G.L., Z.Z., H.P., W.L. and S.Z.; methodology by G.L., H.P. and S.Z. All authors have read and agreed to the published version of the manuscript.

Funding: This work was supported by the National Natural Science Foundation of China (21976078, 22276086), the Natural Science Foundation of Jiangxi Province (20202ACB213001), Hubei Provincial Natural Science Foundation of China (2020CFA096), all of which are gratefully acknowledged by the authors.

Data Availability Statement: The data are contained within the article.

Conflicts of Interest: The authors declare no conflict of interest.

References

1. Lu, Z.S.; Meng, S.J.; Ma, Z.Y.; Yang, M.X.; Ma, D.W.; Yang, Z.X.; Talib, S.H. Electronic and catalytic properties of Ti single atoms@SnO₂ and its implications on sensing mechanism for CO. *Appl. Surf. Sci.* **2022**, *594*, 153500. [[CrossRef](#)]
2. May, Y.A.; Wang, W.W.; Yan, H.; Wei, S.; Jia, C.J. Insights into facet-dependent reactivity of CuO–CeO₂ nanocubes and nanorods as catalysts for CO oxidation reaction. *Chin. J. Catal.* **2020**, *41*, 1017–1027. [[CrossRef](#)]
3. Qian, C.Y.; Bian, J.W.; Ju, F.; Ling, H. Effect of PdS_x on sulfur resistance of Pd-Based catalysts for CO oxidation. *Ind. Eng. Chem. Res.* **2023**, *62*, 3038–3049. [[CrossRef](#)]
4. Zhang, X.D.; Zhang, X.L.; Song, L.; Hou, F.L.; Yang, Y.Q.; Wang, Y.X.; Liu, N. Enhanced catalytic performance for CO oxidation and preferential CO oxidation over CuO/CeO₂ catalysts synthesized from metal organic framework: Effects of preparation methods. *Int. J. Hydrogen Energy* **2018**, *43*, 18279–18288. [[CrossRef](#)]
5. Twigg, M.V. Catalytic control of emissions from cars. *Catal. Today* **2011**, *163*, 33–41. [[CrossRef](#)]
6. Xiang, G.H.; Zhao, S.; Wei, C.D.; Liu, C.Y.; Fei, H.L.; Liu, Z.G.; Yin, S.F. Atomically dispersed Au catalysts for preferential oxidation of CO in H₂-rich stream. *Appl. Catal. B Environ.* **2021**, *296*, 120385–120396. [[CrossRef](#)]
7. Xin, Y.; Zhang, N.N.; Lv, Y.N.; Wang, J.; Li, Q.; Zhang, Z.L. Room-Temperature CO oxidative coupling for oxamide production over interfacial Au/ZnO catalysts. *ACS Catal.* **2023**, *13*, 735–743.
8. Liu, Q.L.; Yang, P.; Tan, W.; Yu, H.W.; Ji, J.W.; Wu, C.; Cai, Y.D.; Xie, S.H.; Liu, F.D.; Hong, S.; et al. Fabricating robust Pt clusters on Sn-Doped CeO₂ for CO oxidation: A deep insight into support engineering and surface structural evolution. *Chem. Eur. J.* **2023**, *29*, 2034–2045.
9. Wu, C.L.; Guo, Z.Z.; Chen, X.Y.; Liu, H. Cu/CeO₂ as efficient low-temperature CO oxidation catalysts: Effects of morphological structure and Cu content. *React. Kinet. Mech. Cat.* **2020**, *131*, 691–706. [[CrossRef](#)]
10. Liu, X.S.; Jin, Z.N.; Lu, J.Q.; Wang, X.X.; Luo, M.F. Highly active CuO/OMS-2 catalysts for low-temperature CO oxidation. *Chem. Eng. J.* **2010**, *162*, 151–157. [[CrossRef](#)]
11. Dae, J.M.; Shin, D.; Jeong, H.; Kim, B.S.; Han, J.W.; Lee, H. Highly Water-Resistant La-doped Co₃O₄ Catalyst for CO oxidation. *ACS Catal.* **2019**, *9*, 10093–10100.
12. Bulavchenko, O.A.; Konovalova, V.P.; Saraev, A.A.; Kremneva, A.M.; Rogov, V.A.; Gerasimov, E.Y.; Afonassenko, T.N. The catalytic performance of CO oxidation over MnO_x-ZrO₂ Catalysts: The role of synthetic routes. *Catalysts* **2022**, *13*, 57–72. [[CrossRef](#)]
13. Liu, Y.N.; Mao, D.S.; Yu, J.; Guo, X.M.; Ma, Z. Low-temperature CO oxidation on CuO-CeO₂ catalyst prepared by facile one-step solvothermal synthesis: Improved activity and moisture resistance via optimizing the activation temperature. *Fuel* **2023**, *332*, 126196. [[CrossRef](#)]
14. Zhao, W.J.; Li, X.; Dang, H.; Wu, R.F.; Wang, Y.Z.; Zhao, Y.X. Effect of Sn addition on the catalytic performance of a Pd-Cu/attapulgite catalyst for room-temperature CO oxidation under moisture-rich conditions. *Reac. Kinet. Mech. Cat.* **2021**, *134*, 759–775. [[CrossRef](#)]
15. Peng, H.G.; Peng, Y.; Xu, X.L.; Fang, X.Z.; Liu, Y.; Cai, J.X.; Wang, X. SnO₂ nano-sheet as an efficient catalyst for CO oxidation. *Chin. J. Catal.* **2015**, *36*, 2004–2010. [[CrossRef](#)]
16. Peng, H.G.; Zhang, X.H.; Han, X.; You, X.J.; Lin, S.X.; Chen, H.; Liu, W.M.; Wang, X.; Zhang, N.; Wang, Z.; et al. Catalysts in coronas: A surface spatial confinement strategy for high-performance catalysts in methane dry reforming. *ACS Catal.* **2019**, *9*, 9072–9080. [[CrossRef](#)]
17. Castillejos, E.; Debouttiere, P.J.; Roiban, L.; Solhy, A.; Martinez, V.; Kihn, Y.; Ersen, O.; Philippot, K.; Chaudret, B.; Serp, P. An efficient strategy to drive nanoparticles into carbon nanotubes and the remarkable effect of confinement on their catalytic performance. *Angew. Chem. Int. Ed. Eng.* **2009**, *48*, 2529–2533. [[CrossRef](#)] [[PubMed](#)]
18. Wang, D.; Yang, G.; Ma, Q.; Wu, M.; Tan, Y.; Yoneyama, Y.; Tsubaki, N. Confinement effect of carbon nanotubes: Copper nanoparticles filled carbon nanotubes for hydrogenation of methyl acetate. *ACS Catal.* **2012**, *2*, 1958–1966. [[CrossRef](#)]
19. Deng, D.H.; Chen, X.Q.; Yu, L. A single iron site confined in a graphene matrix for the catalytic oxidation of benzene at room temperature. *Sci. Adv.* **2015**, *1*, 1500462. [[CrossRef](#)] [[PubMed](#)]
20. Baudouin, D.; Szeto, K.C.; Laurent, P.; Mallmann, A.D.; Fenet, B.; Veyre, L.; Rodemerck, U.; Coperet, C.; Thieuleux, C. Nickel-silicide colloid prepared under mild conditions as a versatile Ni precursor for more efficient CO₂ reforming of CH₄ catalysts. *J. Am. Chem. Soc.* **2012**, *134*, 20624–20627. [[CrossRef](#)] [[PubMed](#)]
21. Bian, Z.; Suryawinata, I.Y.; Kawi, S. Highly carbon resistant multicore-shell catalyst derived from Ni-Mg phyllosilicate nanotubes@silica for dry reforming of methane. *Appl. Catal. B Environ.* **2016**, *195*, 1–8. [[CrossRef](#)]
22. Zhang, X.H.; Zhang, L.; Peng, H.G.; You, X.; Peng, C.; Xu, X.; Liu, W.M.; Fang, X.; Wang, Z.; Zhang, N.; et al. Nickel nanoparticles embedded in mesopores of AlSBA-15 with a perfect peasecod-like structure: A catalyst with superior sintering resistance and hydrothermal stability for methane dry reforming. *Appl. Catal. B Environ.* **2018**, *224*, 488–499. [[CrossRef](#)]
23. Liu, D.; Quek, X.Y.; Cheo, W.N.E.; Lau, R.; Borgna, A.; Yang, Y. MCM-41 supported nickel-based bimetallic catalysts with superior stability during carbon dioxide reforming of methane: Effect of strong metal-support interaction. *J. Catal.* **2009**, *266*, 380–390. [[CrossRef](#)]
24. Dadras, J.; Jimenez-Izal, E.; Alexandrova, A.N. Alloying Pt Sub-nano-clusters with boron: Sintering preventative and coke antagonist. *ACS Catal.* **2015**, *5*, 5719–5727. [[CrossRef](#)]
25. Cai, W.; Zhong, Q.; Zhao, W.; Bu, Y. Focus on the modified Ce_xZr_{1-x}O₂ with the rigid benzene-muti-carboxylate ligands and its catalysis in oxidation of NO. *Appl. Catal. B Environ.* **2014**, *158*, 258–268. [[CrossRef](#)]

26. Feng, B.; Shi, M.; Liu, J.X.; Han, X.C.; Lan, Z.J.; Gu, H.J.; Wang, X.X.; Sun, H.M.; Zhang, Q.X.; Li, H.X.; et al. An efficient defect engineering strategy to enhance catalytic performances of Co₃O₄ nanorods for CO oxidation. *J. Hazard. Mater.* **2020**, *394*, 122540. [[CrossRef](#)]
27. Wang, Y.; Liu, C.; Liao, X.; Liu, Y.; Hou, J.; Pham-Huu, C. Enhancing oxygen activation on high surface area Pd-SnO₂ solid solution with isolated metal site catalysts for catalytic CH₄ combustion. *Appl. Surf. Sci.* **2021**, *564*, 150368. [[CrossRef](#)]
28. Zhang, G.; Han, W.; Zhao, H.; Zong, L.; Tang, Z. Solvothermal synthesis of well-designed ceria-tin-titanium catalysts with enhanced catalytic performance for wide temperature NH₃-SCR reaction. *Appl. Catal. B Environ.* **2018**, *226*, 117–126. [[CrossRef](#)]
29. Bratan, V.; Munteanu, C.; Hornoiu, C.; Vasile, A.; Papa, F.; State, R.; Preda, S.; Culita, D.; Ionescu, N.I. CO oxidation over Pd supported catalysts—In situ study of the electric and catalytic properties. *Appl. Catal. B Environ.* **2017**, *207*, 166–173. [[CrossRef](#)]
30. Wang, Z.; Huang, Z.; Brosnahan, J.T.; Zhang, S.; Guo, Y.; Guo, Y.; Wang, L.; Wang, Y.; Zhan, W. Ru/CeO₂ Catalyst with Optimized CeO₂ Support Morphology and Surface Facets for Propane Combustion. *Environ. Sci. Technol.* **2019**, *53*, 5349–5358. [[CrossRef](#)]
31. Lu, Z.; Ma, D.; Yang, L.; Wang, X.; Xu, G.; Yang, Z. Direct CO oxidation by lattice oxygen on the SnO₂ (110) surface: A DFT study. *Phys. Chem. Chem. Phys.* **2014**, *16*, 12488–12494. [[CrossRef](#)] [[PubMed](#)]
32. Liu, J.; Ji, Q.; Imai, T.; Ariga, K.; Abe, H. Sintering-Resistant Nanoparticles in Wide-Mouthed Compartments for Sustained Catalytic Performance. *Sci. Rep.* **2017**, *7*, 41773. [[CrossRef](#)] [[PubMed](#)]
33. Polshettiwar, V.; Cha, D.; Zhang, X.; Basset, J.M. High-surface-area silica nanospheres (KCC-1) with a fibrous morphology. *Angew. Chem. Int. Ed. Engl.* **2010**, *49*, 9652–9656. [[CrossRef](#)] [[PubMed](#)]
34. Zhao, X.Y.; Ren, X.Y.; Wang, Y.J.; Cao, J.P.; He, Z.M.; Yao, N.Y.; Bai, H.C.; Cong, H.L. Conversion of lignite-derived volatiles into aromatics over Zn@MCM-41 and ZSM-5 tandem catalysts with a high stability. *Fuel* **2023**, *339*, 127430. [[CrossRef](#)]
35. Kohn, W.; Sham, L.J. Self-Consistent equations including exchange and correlation effects. *Phys. Rev.* **1965**, *140*, 1133–1138. [[CrossRef](#)]
36. Dong, W.; Kresse, G.; Furthmüller, J.; Hafner, J. Chemisorption of H on Pd (111): An ab initio approach with ultrasoft pseudopotentials. *Phys. Rev. B Condens. Matter.* **1996**, *54*, 2157–2166. [[CrossRef](#)]
37. Kresse, G.; Furthmüller, J. Efficiency of Ab-initio total energy calculations for metals and semiconductors using a plane-wave basis set. *Comp. Mater. Sci.* **1996**, *6*, 15–50. [[CrossRef](#)]
38. Hammer, B.; Hansen, L.B.; NoRskov, J.K. Improved adsorption energetics within density-functional theory using revised Perdew-Burke-Ernzerhof functionals. *Phys. Rev. B* **1999**, *59*, 7413–7421. [[CrossRef](#)]
39. Perdew, J.P.; Burke, K.; Ernzerhof, M. Generalized gradient approximation made simple. *Phys. Rev. Lett.* **1996**, *77*, 3865–3868. [[CrossRef](#)]
40. Neugebauer, J.; Scheffler, M. Adsorbate-substrate and adsorbate-adsorbate interactions of Na and K adlayers on Al (111). *Phys. Rev. B Condens. Matter.* **1992**, *46*, 16067–16080. [[CrossRef](#)]

Disclaimer/Publisher’s Note: The statements, opinions and data contained in all publications are solely those of the individual author(s) and contributor(s) and not of MDPI and/or the editor(s). MDPI and/or the editor(s) disclaim responsibility for any injury to people or property resulting from any ideas, methods, instructions or products referred to in the content.